In vivo determination of optical properties of normal and tumor tissue with white light reflectance and an empirical light transport model during endoscopy

P. R. Bargo
Oregon Health and Science University
Biomedical Engineering Department
20000 NW Walker Road
Beaverton, Oregon 97006

S. A. Prahl
Oregon Health and Science University
Biomedical Engineering Department
20000 NW Walker Road
Beaverton, Oregon 9700
    and
Providence Saint Vincent Medical Center
Oregon Medical Laser Center
9205 SW Barnes Rd.
Portland, Oregon 97225

T. T. Goodell
Oregon Health and Science University
Biomedical Engineering Department
20000 NW Walker Road
Beaverton, Oregon 9700

R. A. Sleven
G. Koval
G. Blair
Providence Saint Vincent Medical Center
Oregon Medical Laser Center
9205 SW Barnes Rd.
Portland, Oregon 97225

S. L. Jacques
Oregon Health and Science University
Biomedical Engineering Department
20000 NW Walker Road
Beaverton, Oregon 9700

Abstract. Determination of tissue optical properties is fundamental for application of light in either therapeutical or diagnostics procedures. In the present work we implemented a spatially resolved steady-state diffuse reflectance method where only two fibers (one source and one detector) spaced 2.5 mm apart are used for the determination of the optical properties. The method relies on the spectral characteristics of the tissue chromophores (water, dry tissue, and blood) and the assumption of a simple wavelength dependent expression for the determination of the reduced scattering coefficient. Because of the probe dimensions the method is suited for endoscopic measurements. The method was validated against more traditional models, such as the diffusion theory combined with adding doubling for *in vitro* measurements of bovine muscle. Mean and standard deviation of the absorption coefficient and the reduced scattering coefficient at 630 nm for normal mucosa were 0.87 ± 0.22 cm^{-1} and 7.8 ± 2.3 cm^{-1}, respectively. Cancerous mucosa had values 1.87 ± 1.10 cm^{-1} and 8.4 ± 2.3 cm^{-1}, respectively. These values are similar to data presented by other authors. Blood perfusion was the main variable accounting for differences in the absorption coefficient between the studied tissues. © *2005 Society of Photo-Optical Instrumentation Engineers.*
[DOI: 10.1117/1.1921907]

Keywords: optical properties; photodynamic therapy; reflectance spectroscopy; optical fiber probe; endoscopy; light transport model.

Paper 04197R received Oct. 15, 2004; revised manuscript received Dec. 23, 2004; accepted for publication Jan. 19, 2005; published online Jun. 16, 2005.

1 Introduction

Determination of tissue optical properties is fundamental for application of light in either therapeutic or diagnostic procedures. Methods to accurately determine optical properties can lead to optical diagnostic tools,[1] improvements in laser surgery,[2,3] quantitative determination of chromophore[4] and fluorophore[5] concentrations, drug pharmacokinetics,[6] as well as improvements in photodynamic therapy (PDT) dosimetry.[7] The latter is of particular interest for this study.

Experimental determination of tissue optical properties has been proposed using different methodologies. Integrating sphere,[3,8–10] frequency-domain diffuse reflectance,[11,12] time-domain diffuse reflectance,[11,13,14] optoacoustics,[15] and spatially resolved steady-state diffuse reflectance[16,17] are among the most widely used. Each technique has its own advantages and disadvantages. In this work we implemented a spatially resolved steady-state diffuse reflectance method where only two fibers (one source and one detector) spaced 2.5 mm apart are used for the determination of the optical properties. The method relies on the spectral characteristics of the tissue chromophores (water, dry tissue, and blood) to determine the absorption coefficient and on a simple wavelength dependent expression ($\mu_s' = a\lambda^{-b}$) (Ref. 18) for the determination of the reduced scattering coefficient. Advantages of using this method are the inexpensive equipment involved and the simplicity of the measurements which allows its use during endoscopic procedures.

2 Theory

When performing the analysis of reflectance measurements one has to decide upon a light transport model to determine how light from the source fiber reaches the collection fiber. A simple approach is to use the diffusion approximation of the

Address all correspondence to Paulo R. Bargo. Present address: Johnson & Johnson CPPW, 199 Grandview Rd., Skillman, NJ 08558; Tel: 908-874-1227; Fax: 908-874-7205; E-mail: pbargo@cpcus.jnj.com

steady-state radiative transport equation and calculate the net flux escaping the sample at a radial distance *r* from the source as demonstrated by Farrell[16] and shown in Eq. (1):

$$R(r) = z_0 \left(\frac{1}{\delta} + \frac{1}{r_1} \right) \frac{e^{-r_1/\delta}}{r_1^2} + (z_0 + 4AD) \left(\frac{1}{\delta} + \frac{1}{r_2} \right) \frac{e^{-r_2/\delta}}{r_2^2},$$

(1)

where $z_0 = 1/(\mu_a + \mu_s')$, $D = z_0/3$, $\delta = \mathrm{sqrt}(D/\mu_a)$, $r_1^2 = z_0^2 + r^2$, $r_2^2 = (z_0 + 4AD)^2 + r^2$ and $A = (1 + r_i)/(1 - r_i)$. The term r_i is the internal reflection due to the refractive indexmismatch at the surface. Walsh (see Ryde)[19] developed an exact analytical expression for the case where n_0 (the refractive index of the medium of the incident ray) is smaller than n_1 (the refractive index of the medium of the transmitted ray) given by Eq. (2):

$$r_i(m) = \frac{1}{2} + \frac{(m-1)(3m+1)}{6(m+1)^2} + \left[\frac{m^2(m^2-1)^2}{(m^2+1)^3} \right] \ln \left(\frac{m-1}{m+1} \right)$$

$$- \frac{2m^3(m^2 + 2m - 1)}{(m^2+1)(m^4-1)}$$

$$+ \left[\frac{8m^4(m^4+1)}{(m^2+1)(m^4-1)^2} \right] \ln(m),$$

(2)

where $m = n_1/n_0$ and $m > 1$ (since $n_0 < n_1$). For the case where $n_0 > n_1$ (e.g., the internal reflection where $n_0 = n_{\mathrm{tissue}} \approx 1.38$ and $n_1 = n_{\mathrm{air}} = 1.0$) one should first calculate $r_i(m')$ assuming $m' = 1/m$ (hence, $m' > 1$) and second use the expression derived by Egan and Hilgaman[20] based on the n^2 law of radiance [Eq. (3)] to calculate $r_i(m)$:

$$r_i(m) = 1 - m^2 [1 - r_i(m')].$$

(3)

A two-fiber Monte Carlo model (described elsewhere)[21] where all the light that reaches the collection fiber face is counted (open circles) shows approximately the same result predicted by the diffusion model (line) as shown in Fig. 1.

In this example the source and collection fibers have diameters of 600 μm. The refractive indices of the sample and top medium (air) were set to 1.33 and 1, respectively, and the refractive index of the fiber was not considered ($n_{\mathrm{fiber}} = 1$). If the refractive index of the optical fiber is set to its typical value of 1.45 a larger flux is collected (Fig. 1, filled circles). The fiber perturbs the medium by introducing a region where the refractive index is greater than the sample, hence, having no critical angle, which increases the escaping flux. To accurately determine the flux collected by the optical fiber, the optical fiber collection efficiency[21,22] must be taken into account. If only the light that reaches the collection fiber within the angle defined by the numerical aperture is used then the net flux coupling into the fiber is approximately 1/10 (Fig. 1, filled diamonds) of that determined by the diffusion model (for numerical aperature=0.39). Moreover, the collection efficiency is dependent on the optical properties of the medium,[21,22] which in addition to the perturbation of the probe caused by its refractive index makes accurate modeling based on analytical approximations or numerical methods difficult. This task is particularly aggravated when probes com-
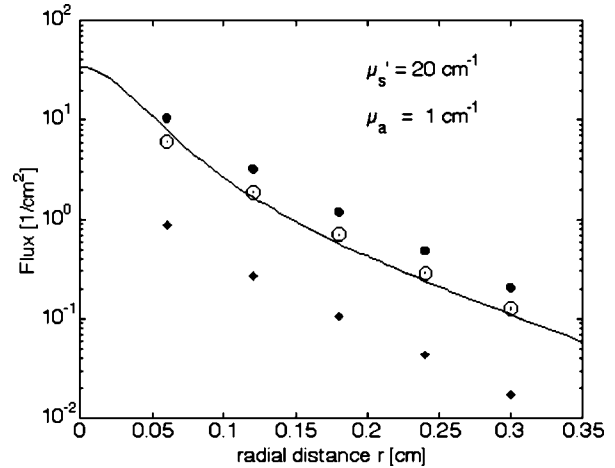

Fig. 1 Comparison of diffusion model [line, Eq. (1)] and Monte Carlo simulations (symbols) of the spatially resolved radiative transport. Empty and filled circles account for light escaping the tissue into the optical fiber face with any escaping angle and n_{fiber} equal to 1 and 1.45, respectively. Filled diamonds account for light escaping the tissue into the optical fiber face within the solid angle determined by the fiber numerical aperture and n_{fiber} equal to 1.45.

posed of more than simple optical fibers are used since the presence of additional material close to the fiber tip (e.g., metal or plastic holders) changes the local boundary conditions. Thus, the assumption of a simple air/medium boundary at the surface becomes flawed. An alternative approach toward characterizing a particular optical fiber device can be based on experimental measurements on optical phantoms with varying absorption and scattering properties to establish an empirical forward light transport model. This paper describe this empirical approach. This calibration technique is specific to the particular geometry of the probe. Any probe design changes require a new calibration.

3 Material and Methods

3.1 *Probe Preparation*

A two-fiber side-firing probe was developed for steady-state diffuse reflectance measurements via the working channel of an endoscope, delivering and collecting light into/from the tissue at 90 deg relative to the axis of the fibers (Fig. 2). Two pieces of 620 μm diameter stainless steel rod were cut 12 mm long and one end of each was polished at a 45° angle to create a mirror. Two lengths of stainless steel tubing (inner diameter =660 μm, outer diameter=830 μm) were cut 8 mm long and a hole was made in each through one side of the tube wall using a 0.025 in. (635 μm diameter) end mill. The holes in the tubing were spaced 2 or 4.5 mm from the end for use as the source or the detector fiber, respectively. The polished steel rods were aligned inside the tubing such that the 45° mirror surface would reflect light through the hole. Two optical fibers (silica–silica, 600 μm core diameter, 3 m long; Ceramoptec Industries Inc., East Longmeadow, MA) were polished flat and one fiber was inserted through the open end of each tube. The optical fiber, rod/mirror, and tube were fixed in place by filling the internal spaces of the tube with clear epoxy (Epo-Tek 301; Epoxy Technology, Billerica, MA), and curing at 60 °C for 4 h. Excess rod was trimmed and filed to remove
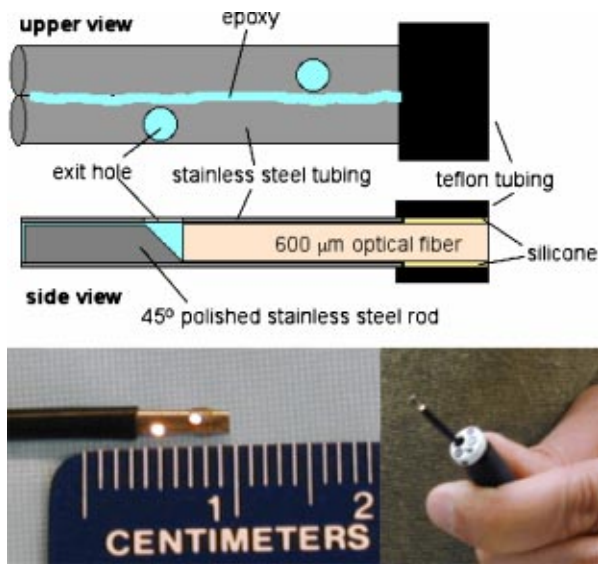
Fig. 4 Typical reflectance raw data for three normal and three tumor sites of esophageal tissue (patient No. E1). A measurement of 2% intralipid is also shown for comparison.

Fig. 2 Top and lower left: Photo and diagram of the two-fiber probe design for reflectance measurements. A 45° polished steel mirror directs source light from one 600 μm optical fiber 90° out the side of the fiber. A second mirror and fiber collect light for detection. Source-collector separation is 2.5 mm. Lower right: the probe is passed through working channel of an endoscope.

sharp edges. The source (with hole 2 mm from the end) and detector (with hole 4.5 mm from the end) were aligned side by side and bonded together by epoxy with the two holes facing toward the same side. The remaining 3 m optical fibers were inserted into Teflon tubing (PTFE 17LW; Zeus Industrial Products Inc., Orangeburg, SC). The tip of the probe was sealed with medical grade silicone glue and a 2 cm piece of heat-shrink Teflon tubing (14HS; Zeus Industrial Products Inc., Orangeburg, SC). The probe was sterilized with ethylene oxide gas prior to patient use.

3.2 Reflectance Measurements

Reflectance measurements of normal and cancerous esophagus, lung, and oral mucosa were taken with the reflectance system shown in Fig. 3. White light from a tungsten lamp (QTH6333, Oriel Instruments, Stratford, CT) was used as the source. The signal was detected with a diode array spectrophotometer (S2000, Ocean Optics Inc., Dunedin, FL). The fiber probe used was described in the previous section.
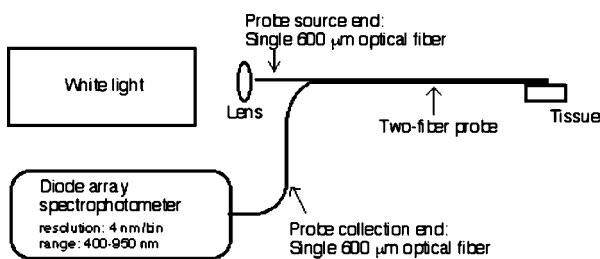

Fig. 3 Reflectance system setup. Light from a tungsten lamp is guided through the two-fiber optical probe. Reflectance spectra is acquired with a spectrophotometer and recorded in a laptop.
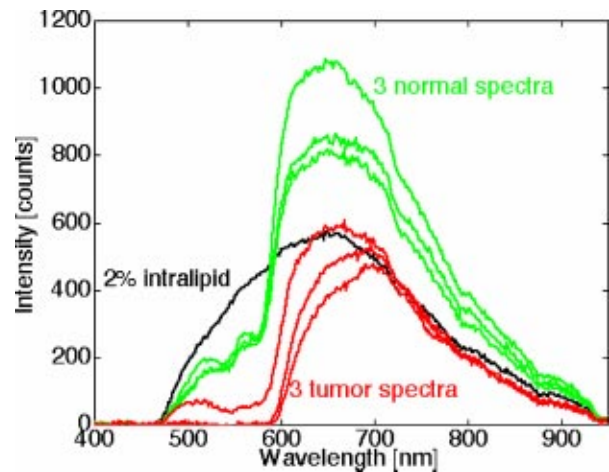
During the clinical procedures the physician positioned the reflectance probe at normal sites (all patients) and tumor sites (PDT patients) according to his clinical evaluation of the tissue. Accurate positioning of the probe was possible due to maneuverability of the endoscope and the fact that a distinct spectrum (Fig. 4) was obtained when proper probe contact was achieved. Typical measurement-to-measurement variation on a single site was approximate 10%. Three sites were measured per patient/disease, and the reflectance spectra were later analyzed to determine the tissue optical properties. The endoscope illumination was turned off while the spectrum for a given site was acquired (200 ms acquisition time). The probe was calibrated by topical placement on an epoxy/titanium-dioxide solid phantom immediately after the procedure. The solid epoxy standard was previously calibrated with integrating sphere measurements and inverse adding-doubling[8,23] modeling to specify its optical properties. Figure 4 shows the raw reflectance spectra for one of the patients. Lower intensities in the 500–600 nm range are due to blood absorption.

3.3 Empirical Forward Light Transport Model

The reflectance spectra used an empirical light transport function determined by experimental calibration of the reflectance probe with a matrix of tissue simulating phantom gels. This experimentally determined transport function behaves similar to that of diffusion theory with a mismatched air/tissue boundary, but accurately accounts for the performance of the actual probe device with its particular geometry and construction as described in the following sections.

3.3.1 Preparation and calibration of the tissue phantom gel matrix

An 8×8 matrix of acrylamide gel tissue simulating phantoms was prepared using Intralipid (Liposin II, Abbott Laboratories, North Chicago, IL) as the scattering element and India ink (No. 4415, Higgs, Lewisburg, TN) as the absorber. The absorption coefficient of the stock ink was determined with an ultraviolet (UV)-visible spectrophotometer (model 8452A, Hewlett-Packard, Palo Alto, CA). A matrix of 64 gels was
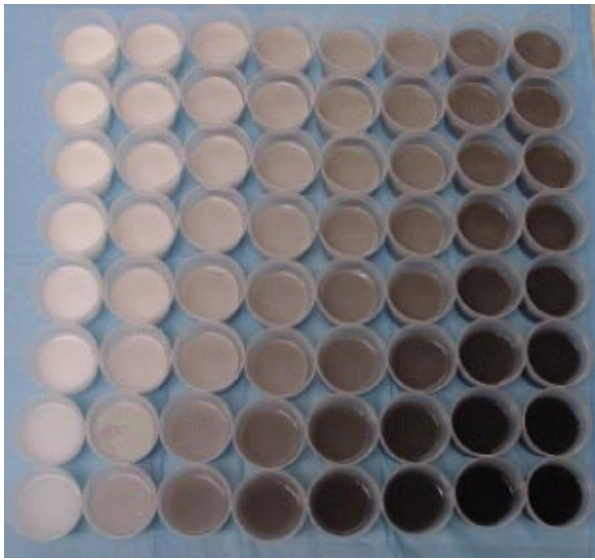
Fig. 5 Picture of the 8×8 acrylamide gel matrix. Rows from top to bottom have final Intralipid concentrations of 7%, 5%, 3.5%, 2.5%, 1.5%, 1.0%, 0.5%, and 0.25%. Columns from left to right have final absorption coefficients at 630 nm of 0.01, 0.1, 0.4, 0.9, 1.6, 2.5, 4.9, and 6.4 cm^{-1}. All samples have 18% acrylamide gel concentration (see text) and a final volume of 100 mL.
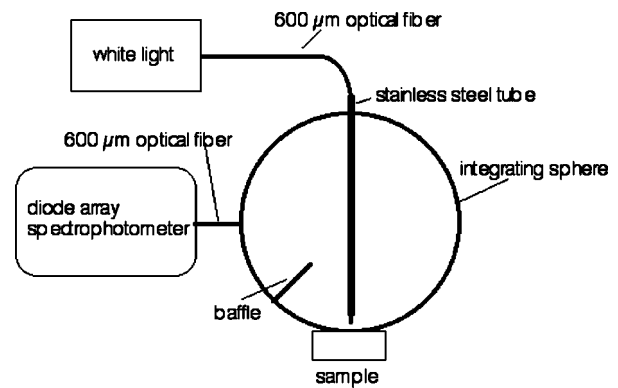

Fig. 6 Setup of the integrating sphere used for calibration of the acrylamide samples. White light from a tungsten halogen lamp is guided through an 600 μm diam optical fiber positoned 5 mm away from the sample, inside the integrating sphere, forming a 3 mm diameter spot. Reflectance spectra is detected through a 600 μm diam optical fiber with a diode array spectrophotometer. Spectralon standards are used to calibrate the reflectance measurements.

prepared with all combinations of eight different reduced scattering coefficients and eight different absorption coefficients. Samples were prepared to yield final Intralipid concentrations of 7%, 5%, 3.5%, 2.5%, 1.5%, 1.0%, 0.5%, and 0.25% (gram lipid/mL solution times 100%). Final range of the gels reduced scattering coefficient at 630 nm was 1–28 cm^{-1}. Different aliquots of India ink were added to yield final absorption coefficients of the gels at 630 nm of 0.01, 0.1, 0.4, 0.9, 1.6, 2.5, 4.9, and 6.4 cm^{-1}. Gels were prepared by adding aliquots of Intralipid, India ink, 45 mL of acrylamide solution (40% concentration) and water to a final volume of 100 mL (4 cm height by 5 cm diameter). The final gel was 18% acrylamide. Stock acrylamide was prepared by diluting 1.4 kg of acrylamide acid (BP170-100, 99%, electrophoresis grade, Fisher Scientific, Pittsburgh, PA) and 35 g of bis-acrylamide (BP171-25, Fisher Scientific, Pittsburgh, PA) in water (1:40 ratio) to create a final volume of 3.5 L (40% concentration). Samples were gelled by adding 0.4 g of ammonium persulfate (BP179-25, Fisher Scientific, Pittsburgh, PA) and 100 μL of TEMED (BP150-20, Fisher Scientific, Pittsburgh, PA) in each 100 mL sample. Figure 5 is a picture of the samples.

Acrylamide did not change the absorbing properties of the added ink (as experimentally verified for an absorbing only gel), however, the scattering properties of the added Intralipid were assumed to change when added to the gels. This assumption was based upon experiments done with samples before and after gelling (data not shown). Optical properties of the final gel samples were determined by measuring the total reflectance with an 8 in. diam integrating sphere (IS-080, Labsphere Inc., North Sutton, NH). Samples were placed directly at the open port (1 in. diam) of the integrating sphere. Illumination of the sample was provided by a 600 μm diam optical fiber positioned inside the integrating sphere through a stainless steel tube 5 mm away from the sample, which yielded a 3

mm diameter spot at the sample surface. Total diffusely reflected light was collected with a 600 μm diam optical fiber positioned in another port of the sphere. A baffle was positioned between the two ports. The setup is shown in Fig. 6.

Measurements of Spectralon standards (Labsphere Inc., North Sutton, NH) were taken to calibrate the sphere. Reduced scattering (μ_s') and absorption (μ_a) coefficients were determined using a combination of the added-absorber[24] and adding-doubling[8,23] methods to predict the total diffuse reflectance (R_i^{AD}) for comparison with the measured total diffuse reflectance (R_i^{EXP}) in a least square minimization routine (Nelder-Mead simplex algorithm). Determination of the two parameters (μ_s' and μ_a) with only one measurement of total diffuse reflectance is possible because of the knowledge of the added absorber to all samples. The minimization was done wavelength-by-wavelength using the samples with the five lowest ink concentrations ($D_i^{\mathrm{ink}} = 0$, 0.0003, 0.0010, 0.0024, 0.0040, corresponding to 0.01, 0.1, 0.4, 0.9, and 1.6 cm^{-1} at 630 nm, respectively) for each Intralipid concentration. Figure 7 shows a flow chart of the minimization.

3.3.2 *Probe calibration*

All 64 acrylamide gel samples and the epoxy/titanium-dioxide solid standard were measured with the probe. A drop of water aided optical coupling between the gel and the optical fiber probe. Measurement-to-measurement variation decreased from approximately 20% without optical coupling to less than 5% with optical coupling.

Reflectance measurements on samples (M_s) were normalized by the epoxy/titanium-dioxide (epoxy-TiO$_2$) solid standard (M_{std}). The final spectrum was the ratio M:

$$M(\lambda) = \frac{M_s(\lambda)}{M_{\mathrm{std}}(\lambda)} = \frac{S(\lambda)R_s(\lambda)\eta_s(\lambda)D(\lambda)}{S(\lambda)R_{\mathrm{std}}(\lambda)\eta_{\mathrm{std}}(\lambda)D(\lambda)}$$

$$= \frac{R_s(\lambda)\eta_s(\lambda)}{R_{\mathrm{std}}(\lambda)\eta_{\mathrm{std}}(\lambda)}, \qquad (4)$$
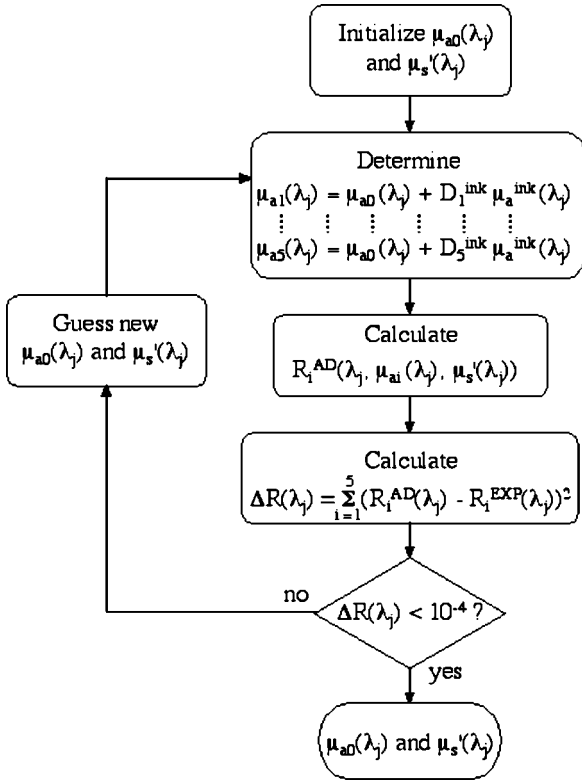
Fig. 7 Flow chart of the minimization process to determine the Intralipid absorption coefficient (μ_{a0}) and the reduced scattering coefficient (μ_s') for each wavelength λ_j and for each Intralipid concentration. The samples with five lowest dilutions of ink ($i=1-5$) were used to determined μ_{a0} and μ_s'. Least square minimization is performed between the reflectance calculated with adding-doubling and the reflectance experimentally measured. Effectively this finds the best μ_{a0} and μ_s' for each wavelength from five measurements on samples with the same scattering coefficient and known differences in absorption.

where $S(\lambda)$ (W) is the light source power, $D(\lambda)$ (counts/W) is the detector sensitivity, $R_s(\lambda)$ (1/cm^2) is the optical transport into the medium and returning to the sample surface at the collection fiber, $\eta_s(\lambda)$ (dimensionless) is the optical fiber collection efficiency for the sample, $\eta_{std}(\lambda)$ (dimensionless) is the optical fiber collection efficiency for the standard, and $R_{std}(\lambda)$ (dimensionless) is the reflectance of the epoxy/titanium-dioxide solid standard (0.65 at 630 nm).

The terms S (the source spectral response) and D (the detector spectral response) are the same for samples and standard measurements and do not vary within a measurement procedure and thus cancel in Eq. (4). The normalized measurement, $M(\lambda)$, was multiplied by the reflectance of the standard $[R_{std}(\lambda)]$ determined with the integrating sphere setup shown in Fig. 6 to yield the adjusted normalized measurement $M^*(\lambda)$ [Eq. (5)]:

$$M^*(\lambda) = \frac{M_s(\lambda)}{M_{std}(\lambda)} R_{std}(\lambda) = R_s(\lambda) \frac{\eta_s(\lambda)}{\eta_{std}(\lambda)}. \quad (5)$$

The term M^* incorporated the actual light transport of the sample multiplied by the ratio between the optical fiber probe collection efficiency for the sample and the standard.

Each phantom gel yielded a spectrum of reflection values ($\lambda=480-925$ nm). With the knowledge of the optical properties of the samples from the integrating sphere measurements a light transport map was generated for each wavelength by interpolating the 64 normalized measurements $[M^*(\lambda_i)]$ as follows:

(a)   The 64 measurements for one wavelength (e.g., $\lambda=630$ nm) were plotted on a grid of absorption (μ_a) and reduced scattering (μ_s') coefficients [Fig. 8(a)].

(b)   A piecewise linear interpolation of the eight adjacent points in the reduced scattering dimension was made using the function *interp*1 in Matlab as shown in Fig. 8(b), i.e., $M^*(\mu_s')$ at each of the eight known μ_a.

(c)   The result of the linear interpolation was plotted on the same grid of absorption (μ_a) and reduced scattering (μ_s') coefficients [Fig. 8(c)].

(d)   The eight adjacent points in the absorption dimension were fitted with an exponential curve [Eq. (6)] as shown in Fig. 8(d):

$$M^*(\mu_a,\mu_s')=C_1(\mu_s')e^{-\mu_a L_1(\mu_s')}+C_2(\mu_s'), \quad (6)$$

where the constants C_1, L_1, and C_2 are a function of the μ_s'.

(e)   The resulting constants C_1, L_1, and C_2 (Fig. 9) were used with Eq. (6) to interpolate the remaining values in the transport map as shown in Fig. 8(e).

To speed the calculation of the light transport the coefficients C_1, L_1, and C_2 were fit to polynomial functions of orders 4, 15, and 15, respectively. The use of high order polynomial functions for L_1 and C_2 was necessary because of the rapid changes in these coefficients as a function of reduced scattering coefficients. Nevertheless, Fig. 9 shows that C_1, L_1, and L_2 were well-behaved functions of μ_s'. Fitted values beyond the limits of maximum and minimum coefficient values were discarded (shadow regions on Fig. 9).

3.4 Modeling of Tissue Reflectance with the Empirical/Spectral Model

The analysis of reflectance assumes (1) that the reduced scattering coefficient of the tissue behaves as a power of the wavelength[18] and (2) that a linear combination of chromophore spectra can fully approximate the absorption coefficient.[18] Tissue absorption was modeled as a linear combination of water (μ_a^{water}), a background spectrum for dry bloodless tissue (μ_a^{dry}), and a variable blood volume fraction (f_v) of oxygenated and deoxygenated whole blood ($\mu_a^{oxy}, \mu_a^{deoxy}$) at an oxygen saturation (SO$_2$). The fraction of water was kept fixed at 75%. In principle, the water content could be fit, but our system was not sufficiently sensitive in the 900–1000 nm spectral region where water strongly influences the spectra.

Tissue scattering can be represented by a simple expression, $a\lambda^{-b}$, that mimics the Mie scattering from larger tissues structures such as collagen fiber bundles, mitochondria, nuclei, and cells.[25] The Rayleigh scattering ($\propto \lambda^{-4}$) was ne-
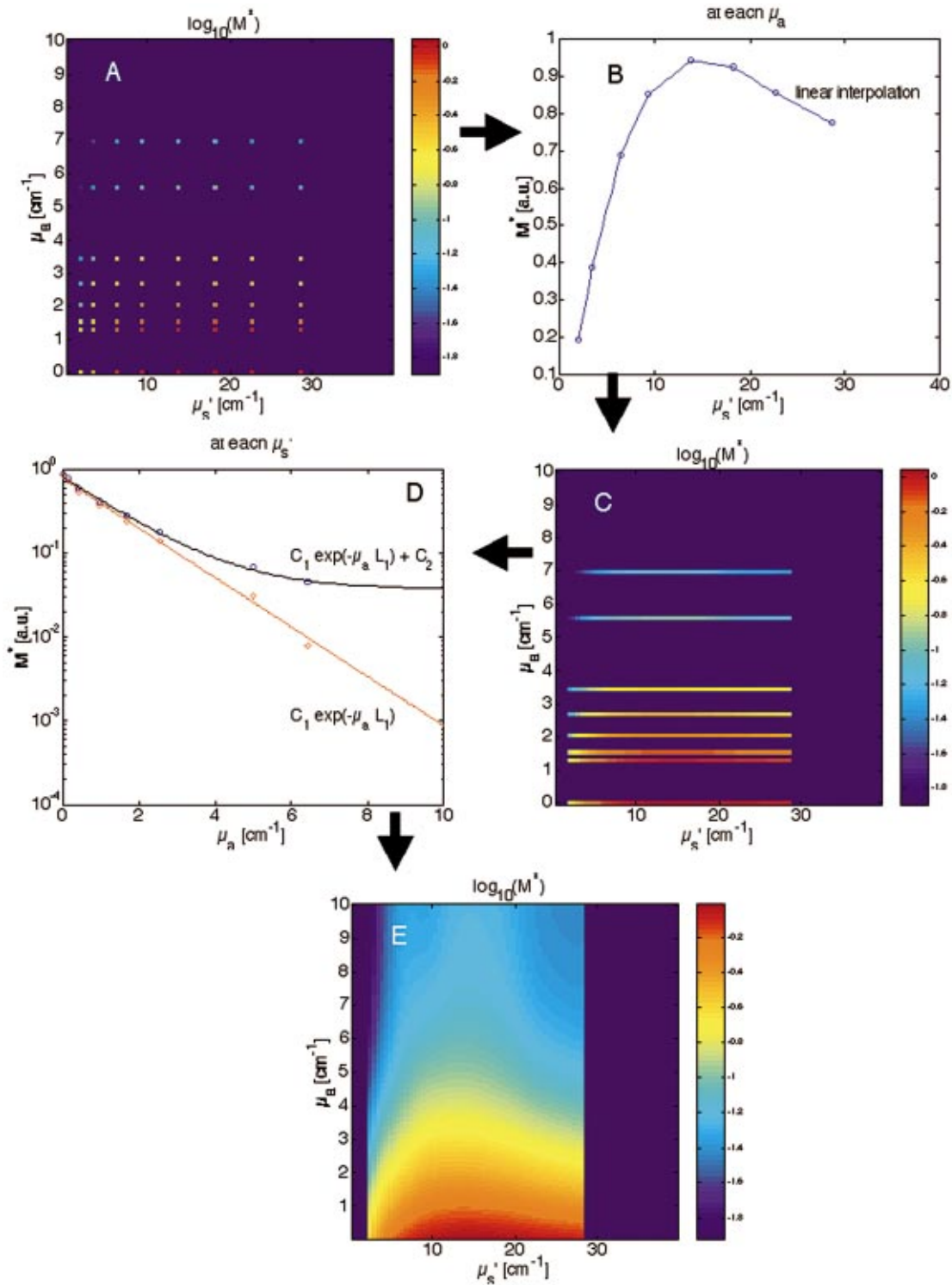
Fig. 8 Creating the light transport maps used as forward model for the reflectance measurements. This is an example for one wavelength (630 nm). (a) Log base 10 of the normalized measurement M^* for the 64 samples at 630 nm displayed in a grid of absorption and reduced scattering coefficient. (b) Linear interpolation of the eight data points with the lowest μ_a in (a). (c) Log base 10 of the normalized measurement M^* obtained from the linear interpolation in (b). The points highlighted by the white line are shown in (d). (d) Exponential fit according to Eq. (6) of data highlighted in (c). (e) Light transport map at 630 nm constructed with the coefficients shown in Fig. 9 and Eq. (6).

Fig. 9 Coefficients C_1, L_1, and C_2 used to reconstruct the map on Fig. 8 (630 nm). The coefficients were fitted to polynomials (lines) to speed the calculation of the light transport.

Fig. 10 Spectra of tissue chromophores used in Eq. (7). Oxy and deoxy spectra are for 45% hematocrit blood.

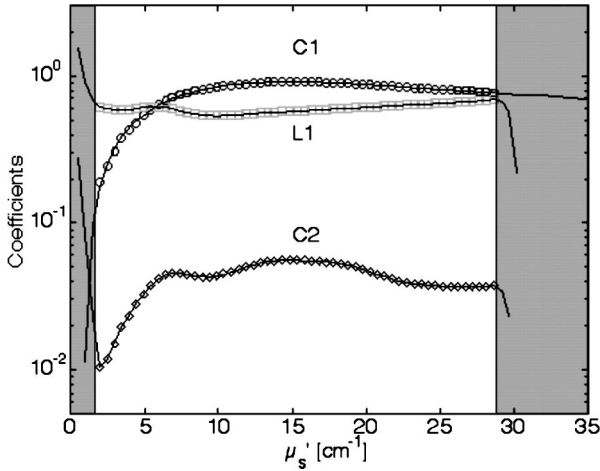glected in this modeling effort because our spectra were acquired above 480 nm and were not sensitive to Rayleigh scattering. The absorption coefficient (μ_a) and reduced scattering coefficient (μ_s') were specified as

$$\mu_a(\lambda) = \mu_a^{dry}(\lambda) + f_W \mu_a^{water}(\lambda) + f_v[SO_2 \mu_a^{oxy}(\lambda)$$
$$+ (1 - SO_2) \mu_a^{deoxy}(\lambda)], \tag{7}$$

$$\mu_s'(\lambda) = a\lambda^{-b}, \tag{8}$$

$$\mu_a^{dry}(\lambda) = A \exp(-B\lambda), \tag{9}$$

where $\mu_a(\lambda)$ (cm^{-1}) is the total absorption coefficient of tissue *in vivo*, $\mu_a^{dry}(\lambda)$ (cm^{-1}) is the absorption coefficient of dry bloodless tissue, $\mu_a^{water}(\lambda)$ (cm^{-1}) is the absorption coefficient of pure water, $\mu_a^{oxy}(\lambda)$ (cm^{-1}) is the absorption of fully oxygenated blood (45% hematocrit), $\mu_a^{deoxy}(\lambda)$ (cm^{-1}) is the absorption of fully deoxygenated blood (45% hematocrit), f_W (dimensionless) is the volume fraction of water, F_v (dimensionless) is the volume fraction of blood in tissue, SO_2 (dimensionless) is the oxygen saturation, A (cm^{-1}) is the amplitude constant for $\mu_a^{dry}(\lambda)$, B (nm^{-1}) is the rate constant for $\mu_a^{dry}(\lambda)$, $\mu_s'(\lambda)$ (cm^{-1}) is the reduced scattering coefficient of tissue *in vivo*, a (cm^{-1}) is the factor that characterizes magnitude of scattering, b (dimensionless) is the factor that characterizes wavelength dependence of scattering, and λ (nm) is the wavelength.

Typical spectra for μ_a^{dry}, μ_a^{water}, and the μ_a^{oxy} and μ_a^{deoxy} for whole blood at 45% hematocrit are shown in Fig. 10.[26]

The absorption of dry tissue was assumed to behave as an exponential decay, as suggested by Saidi.[27] This approximation was used to represent the sum of the effect that all chromophores with Soret band in the UV-blue spectral region (e.g., collagen fibers, bilirubin, porphyrins, etc.) have on the absorption coefficient in the visible range.

Measurements on the solid standard made of epoxy, titanium dioxide (TiO$_2$) and ink used to normalize the acrylamide gel phantoms (Sec. 3.3.2.) were taken to correct for

day-to-day variations in the wavelength and magnitude dependence of the light source and detector sensitivity. As an example, normalized data from Fig. 4 is presented in Fig. 11.

In effect six parameters were determined from each reflectance spectrum by a least square minimization. The fitting process consisted of two phases. First, only the measurements at the isosbestic points (500, 530, 545, 570, 584, 796 nm) were used (so that oxygen saturation is unimportant) to determine a, b, blood fraction (f_v), A, and B. This produced a value for b that was held constant in the second fitting and optimized initial guesses for a, blood fraction (f_v), A and B. The second fitting allowed a, blood fraction (f_v), blood oxygen saturation (SO_2), A and B to vary and used the entire reflection spectrum. Specifically,

(a)   Variables a, b, f_v, A, and B are initialized.

(b)   The parameters μ_a and μ_s' are determined using

Fig. 11 Data from Fig. 4 normalized by the measurement of the epoxy standard (M_{std}) and multiplied by the standard reflectance (R_{std}) as an example of the normalization given by Eq. (6) to yield M^*.

Eqs. (7), (8), and (9) for the isosbestic wavelengths (500, 530, 545, 570, 584, 796 nm) and assuming $SO_2 = 1$.
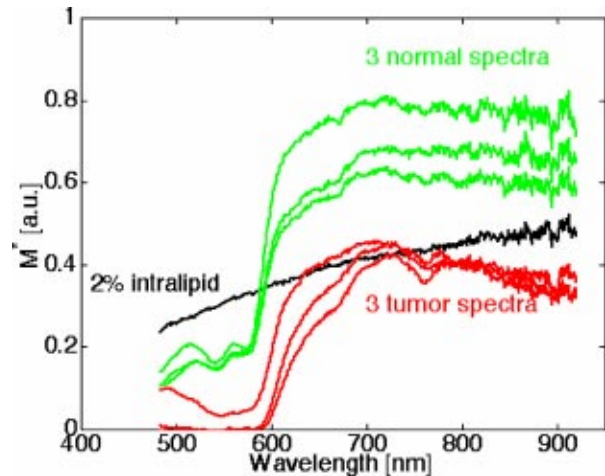
(c) The predicted normalized measurement $[M_p^*(\lambda)]$ was calculated for the isosbestic wavelengths.

(d) $M_p^*(\lambda)$ was compared to the experimental normalized measurement from the patient $[M_{exp}^*(\lambda)]$ in a least square minimization process of a, b, f_v, A, and B.

(e) Once a, b, f_v, A, and B were minimized with respect to the isosbestic wavelengths, the value of b was held constant. The minimized values of a, f_v, A, and B were used as starting point to the second phase of the minimization where these variables plus the SO_2 were allowed to vary.

(f) The parameters μ_a and μ_s' are determined using Eqs. (7), (8), and (9) for the all wavelengths.

(g) Using the empirical transport model, $M_p^*(\lambda)$ was calculated wavelength-by-wavelength.

(h) $M_p^*(\lambda)$ was compared to $M_{exp}^*(\lambda)$ for all wavelengths in a least square minimization process of a, f_v, SO_2, A, and B.

3.5 Validation of the Empirical Model with a Diffusion Model

Measurements of bovine muscle were made to validate the model. An *in vitro* tissue measurement was preferred to the use of phantoms composed of scatters such as intralipid or microspheres and absorbers such as India ink or other chemical chromophores because of the model dependence on the spectra of the tissue components (oxy and deoxy blood, water, etc.). Bovine muscle was bought fresh from the local abattoir and was approximately 24 h postmortem at the time of the measurements. Tissue was kept refrigerated and wrapped in plastic until the time of use. Three sites in three different samples were measured.

Optical properties of the samples were determined using the empirical model described in the previous sections and compared to optical properties determined by a wavelength-by-wavelength model using the total diffuse reflectance measurement (R_t) in conjunction to a spatially resolved steady-state diffuse reflectance measurement (R_d). The measurement R_t was done with the integrating sphere setup shown in Fig. 6. The measurement of R_d was made with an optical fiber probe composed of five 400 μm diam optical fibers linearly spaced 1.524 mm (0.060 in.) apart. The first fiber was used to illuminate the tissue with a white light tungsten lamp (QTH6333, Oriel Instruments, Stratford, CT). The remaining four fibers were connected to a four-channel diode array spectrophotometer (S2000, Ocean Optics Inc., Dunedin, FL). A measurement of the epoxy-TiO$_2$ standard referred on Sec. 3.3.2 was taken to normalize the tissue measurements. This normalization was done to cancel the source and detector spectral variation. Optical properties were determined by fitting the experimental measurements R_t and R_d to adding-doubling[8,24] and diffusion theory[16,28] models, respectively, wavelength-by-wavelength, as follows:

(a) Initialize $\mu_a(\lambda_0)$, $\mu_s'(\lambda_0)$, and const(λ_0) for a

wavelength λ_0 (e.g., 630 nm). The variable const was used as a multiplication factor in Eq. (1) to account for the optical fiber collection efficiency.

(b) Calculate the predicted total diffuse reflectance $pR_t(\lambda_0)$ using the initial μ_a, μ_s', and the adding-doubling model.

(c) Calculate the predicted spatially resolved diffuse reflectance $pR_d(\lambda_0)$ at each of the four distances using the initial μ_a, μ_s', and Eq. (1). The normalization is obtained by multiplying $pR_d(\lambda_0)$ by const(λ_0) and divide by the spatially resolved diffuse reflectance of the epoxy-TiO$_2$ standard [which is calculated with the known optical properties of the standard at $\lambda = \lambda_0$ and Eq. (1)].

(d) Compare $pR_t(\lambda_0)$ to $R_t(\lambda_0)$ and $pR_d(\lambda_0)$ to $R_d(\lambda_0)$ in a least square minimization of $\mu_a(\lambda_0)$, $\mu_s'(\lambda_0)$, and const(λ_0) using Eq. (10):

$$e = \sqrt{\{[pR_t(\lambda_0) - R_t(\lambda_0)]/R_t(\lambda_0)\}^2} + \sqrt{\sum_k \{[pR_d(\lambda_0, r_k) - R_d(\lambda_0, r_k)]/R_d(\lambda_0, r_k)\}^2},$$

(10)

where e is the function to be minimized and r_k are the radial position of the collection fibers.

3.6 Patients

Patients undergoing endoscopic screening for esophageal diseases and patients undergoing photodynamic therapy for esophageal, lung, and oral cavity cancer treatment were recruited for the reflectance measurements. Consent to take part in the study was obtained from all patients. A study protocol was defined and approved by the Providence St. Vincent Medical Center IRB Committee. Detailed written and oral information on the study protocol was given to the patients prior to enrollment. The measurements increased the endoscopic procedure an average of 5 min.

A total of nine patients (Nos. N1–N9) undergoing the endoscopic procedures for screening purpose were recruited to set base line values for optical properties at clinically evaluated normal tissue sites. One measurement was taken at three different sites for each patient.

Four patients with esophageal tumors (Nos. E1–E4), two patients with lung tumors (Nos. L1–L2) and one patient with oral cavity tumors (No. O1) scheduled to receive standard FDA and off-label PDT treatment protocols were recruited for this study. All were intravenously injected with 2 mg/(kg body weight) of Photofrin II (Axcan Pharma Inc., Birmingham, AL) 48 h prior to activation by 630 nm laser light. Measurements of reflectance spectra were taken immediately prior to light treatment. Three clinically evaluated normal sites and three clinically evaluated tumor sites were measured per patient. Exception was lung patient No. L2, who had only two normal sites and three tumor sites measured due to time constraint.
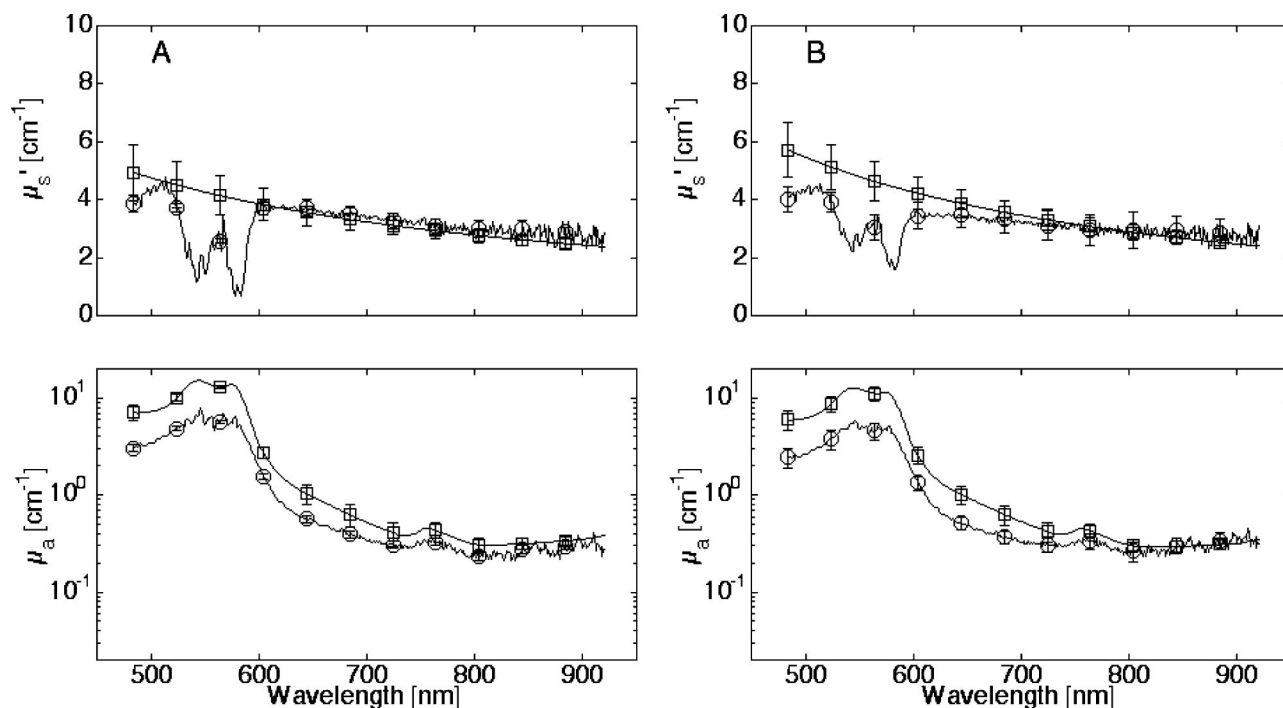
Fig. 12 Reduced scattering (μ_s', top) and absorption (μ_a, bottom) coefficients determined for bovine muscle determined by the empirical/spectral model (diamonds) in comparison to the optical properties determined by the wavelength-by-wavelength model described in section 3.5 (circles). (a) Average and standard deviations for three different sites measured at one sample. (b) Average and standard deviations for all sites measured (three sites per sample for three different samples).

4 Results

4.1 Bovine Muscle in vitro

Comparison between the optical properties of bovine muscle determined with the empirical/spectral model and by the wavelength-by-wavelength model (Sec. 3.5) is shown in Fig. 12. Figure 12(a) shows the average and standard deviations for μ_s' (top) and μ_a (bottom) obtained with the two techniques for three different sites of one sample. Similar results are shown in Fig. 12(b) for all nine sites measured (three sites times three samples). These results illustrate how the analysis using the empirical/spectral model yielded a smooth spectrum for the reduced scattering coefficient while the analysis using the diffusion theory/wavelength-by-wavelength model allowed for cross talk between the absorption and scattering (seen as the influence of hemoglobin absorption in the reduced scattering coefficient spectrum). Note, however, that at longer wavelengths where hemoglobin absorption is low, the reduced scattering coefficient was similar for both methods.

4.2 Human Tissue in vivo

Figure 13 shows results of the empirical/spectral model for esophageal PDT patient No. E1 with plots of the experimental and predicted spectra for three normal sites [Figs. 13(a)–13(c)] and three tumor sites [Figs. 13(d)–13(f)]. Experimental curves in Figs. 13(a)–13(f) are the same shown in Fig. 9. Bloodless tissue curves are shown in black dashed lines, based on setting the factor f_v equal to zero for μ_a in Eq. (7) and determining the light transport using the bloodless tissue optical properties and Eq. (8). The values of a, b, f_v, SO_2, A, and B are specified in the graphs for this patient and in Tables

1, 2, and 3 for sites measured in all patients (PDT and non-PDT). To obtain the optical properties one must use these numbers with Eqs. (7), (8), and (9). The normalized residual error [(predicted−experimental)/experimental] is also shown.

In some cases the blood content from tumor tissue was so high that zero reflectance was obtained in the 500–600 nm wavelength range. In these cases data were truncated below 600 nm and the same fitting algorithm was attempted. Without the data below 600 nm, the fitting for a and b (that describe the reduced scattering coefficient) and B (that describe the absorption of dry tissue) did not always converge to values that represented physiological values of μ_s' and μ_a. Therefore, the values of a, b, and B were determined using the average of μ_s' and μ_a^{dry} from the other tumor sites for the same patient and the variables f_v, SO_2, and A were fitted using the data above 600 nm. In the case of patient No. E1, just one tumor measurement (tumor site No. 1) did not have zero reflectance values in the 500–600 nm wavelength range. Thus, the values of a, b, and B for this tumor site were used to determine the other variables (f_v, SO_2, and A) for tumor site Nos. 2 and 3. The sites where truncated data were used are highlighted in Table 3.

Calculated reduced scattering and absorption coefficients of normal and tumor sites for patient No. E1 are shown in Figs. 14(a) and 14(b), respectively. Reduced scattering coefficients for all three tumor sites are identical since the same values of a and b were assumed for all sites as explained earlier.

Absorption and reduced scattering coefficients and the optical penetration depth (δ) at 630 nm are shown in Tables 1, 2, and 3 for all patients. Histograms of the optical penetration
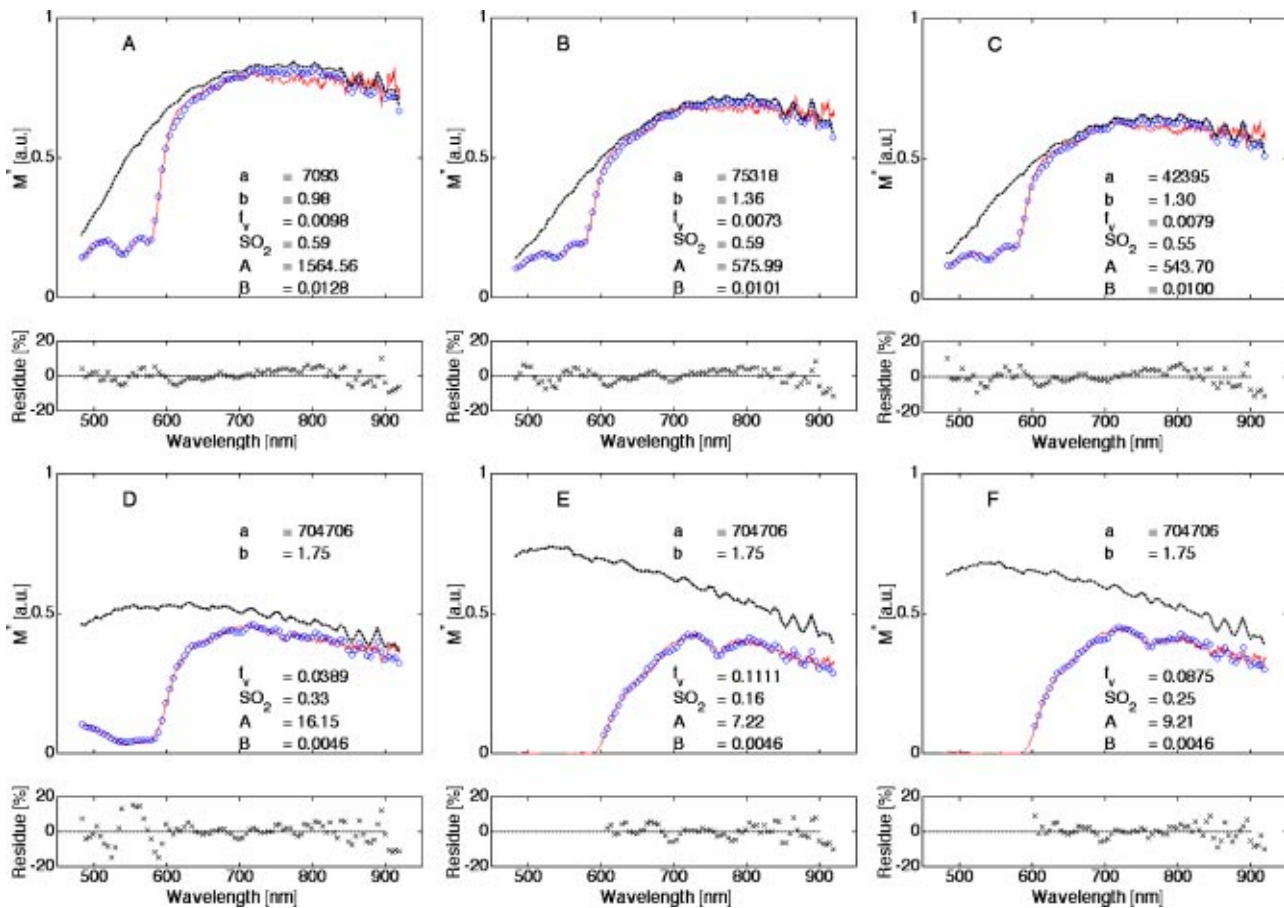
Fig. 13 Normalized data for normal site 1–3 and tumor sites 1–3 of patient No. E1 in comparison to the predicted values (circles) determined using the fitted parameters a, b, f_v, SO_2, A, and B shown, and Eqs. (7), (8), and (9). The percentage residual errors [(predicted−measured)/measured times 100%] are shown below each curve. Bloodless tissue curves are shown in black dashed lines, based on setting the factor f_v equal to zero for μ_a in Eq. (7). The system was not able to record data below 600 nm for tumor sites 2 and 3 because of strong blood absorption in that spectral range. Only data above 600 nm was used for fitting. Values of a, b, and B were assumed to be the same as those for tumor site 1 (see text).

depth at 630 nm are shown in Fig. 15 for the normal, PDT normal and PDT tumor.

Mean and standard deviations for blood fraction (f_v), blood oxygen saturation (SO_2), and reduced scattering coefficients (μ_s'), absorption coefficients (μ_a), and optical penetration depths (δ) at 630 nm are shown in Table 4.

Two-sample t tests[29] were performed to compare results for normal esophageal tissue of non-PDT against normal tissue of PDT patients. t tests were also performed to compare normal against tumor sites for PDT patients. Significant difference was found between non-PDT normal and PDT normal tissue for f_v and SO_2 with p values <0.03 and <0.01, respectively. No significant difference was found for the other parameters. Comparison between PDT normal and PDT tumor sites showed significant difference between all parameters except μ_s' with p values <0.02, <0.003, <0.001, and <0.002 for f_v, SO_2, μ_a, and δ, respectively.

5 Discussion

One of the big challenges in making endoscopic measurements is the size constraint imposed on the optical fiber probe. The typical diameter of the working channel for commercial endoscopes is 2–3 mm.[30] Our first attempt was to use a single bare 600 μm diam optical fiber for both delivery and collection of light (data not shown). Unfortunately the sampling volume of this fiber configuration limits its ability to determine the absorption coefficient because the pathlength of collected photons was too short.[31] Furthermore, when using a single fiber the specular reflection of the optical fiber tip is an important component of the detected signal and fiber-tissue contact becomes an important issue, increasing the variation in the data.[32] An alternative approach for the endoscopic measurements was the development of the two-fiber probe described in Sec. 3.1. This probe used two fibers, one as source and the other as detector, separated 2.5 mm apart in a side viewing configuration, which allowed a greater sampling volume and eliminated fiber specular reflection on the detected signal.

The empirical model of Sec. 3.3 lead to the use of a probe specific model, rather than the use of a theoretical model (such as diffusion theory or Monte Carlo simulations) that attempted to adequately model the geometry and boundary conditions of the probe. Figure 1 shows the impact of different boundaries on the detected signal of a Monte Carlo simulation when an ideal optical fiber is used to collect light from a semi-infinite medium. The optical fiber index of refraction

Table 1 Values of a, b, f_v, SO_2, A, B, and optical properties at 630 nm for normal sites of non-PDT patients.

Patent No.	Site	a (cm^{-1})	b (-)	f_v (%)	SO_2 (%)	A (cm^{-1})	B (nm^{-1})	$\mu_s'^{630}$ (cm^{-1})	μ_a^{630} (cm^{-1})	δ^{630} (mm)
	1	19 246	1.22	1.83	54	409	0.011	7.4	0.71	2.4
N1	2	52 738	1.39	3.09	67	326	0.010	7.0	0.94	2.1
	3	30 888	1.32	1.33	44	1094	0.013	6.2	0.59	2.9
	1	277 950	1.56	4.98	39	0.51	0.000	12.0	1.40	1.3
N2	2	14 057	1.19	1.73	40	9681	0.017	6.4	0.56	2.9
	3	251 580	1.64	0.69	42	231	0.009	6.5	0.85	2.3
	1	8994	1.10	1.92	49	4966	0.015	7.5	0.64	2.5
N3	2	2904	1.00	1.57	49	6950	0.016	4.7	0.50	3.6
	3	6310	1.05	2.42	70	2698	0.014	7.5	0.64	2.5
	1	48 580	1.37	1.33	61	361	0.010	7.0	0.67	2.6
N4	2	118 056	1.53	1.49	66	293	0.010	6.3	0.80	2.4
	3	308 977	1.62	0.63	52	82	0.007	8.9	0.94	1.9
	1	108 754	1.47	1.03	51	3234	0.014	8.1	0.60	2.5
N5	2	144 963	1.46	3.55	37	5 142 700	0.028	11.9	0.74	1.9
	3	69 965	1.40	0.84	44	2055	0.013	8.3	0.72	2.3
	1	54 916	1.38	1.46	58	683	0.011	7.3	0.82	2.2
N6	2	10 312	1.12	1.58	48	1911	0.013	7.4	0.72	2.4
	3	93 179	1.45	1.84	55	1117	0.012	8.1	0.72	2.3
	1	184 459	1.55	1.07	53	97	0.008	8.7	0.83	2.0
N7	2	143 323	1.50	0.99	53	44	0.006	8.8	1.10	1.7
	3	11 139	1.15	0.90	45	361	0.011	6.6	0.55	2.9
	1	421 423	1.69	2.00	58	72	0.007	7.7	1.20	1.8
N8	2	321 110	1.64	1.38	54	36	0.005	8.4	1.35	1.6
	3	207 327	1.59	0.92	58	606	0.011	7.4	0.89	2.1
	1	183 263	1.56	2.19	71	313	0.010	7.6	0.84	2.2
N9	2	214 786	1.63	2.12	59	1643	0.013	6.0	0.71	2.6
	3	119 723	1.49	1.63	72	324	0.010	8.1	0.67	2.4

perturbs the medium boundary and the optical fiber numerical aperture limits the fiber cone of collection. With an actual optical fiber probe the material surrounding the optical fiber (i.e., metal supports, plastic tubing) will aggravate the changes in the medium boundary. Furthermore, the optical fiber collection efficiency[21,22] is a function of the tissue optical properties, which adds more complexity to the model. Since the empirical model is based on measurements with the actual probe in samples with known optical properties all these issues get lumped together in the transport function. The disadvantage is the fact that the model is specific for a particular probe and in principle calibration has to be done for each probe that is made. Normalization of the data and the model by the measurement of a solid standard (also used to account for day-to-day variations in the system) helped overcome this calibration issue as long as the probes have the same design.

The ability to determine two parameters, the reduced scattering coefficient (μ_s') and the absorption coefficient (μ_a), with one spectral reflectance measurement is only possible because of the spectral nature of the tissue components and the assumptions stated in Eqs. (7), (8), and (9). In a typical experimental setup two independent (or orthogonal) measurements have to be made to determine two independent variables. In our case we only have one measurement, but composed of more than 400 spectral points (approximate one point per nanometer) that are not completely independent of each other. Nevertheless there exists enough information to derive the two optical properties if *a priori* information about the tissue components is known. For this we assume that the tissue absorption coefficient is composed of absorption from dry tissue (μ_a^{dry}), water (μ_a^{water}), oxy- and deoxy-blood (μ_a^{oxy} and μ_a^{deoxy}) and that the reduced scattering coefficient behaved as $a\lambda^{-b}$.

As with any fitting routine, starting with the appropriate initial values for the fitting parameters helps avoiding reaching local minima (which leads to incorrect answers) in the minimization routine. Using the isosbestic spectral points and leaving the blood oxygen saturation (SO_2) out of the initial fitting helped the appropriate determination of the parameter b for the reduced scattering as well as establishing better guesses for the other initial parameters. In a few cases the determination of b with the limited number of data points (the isosbestic points) resulted in nonphysiological values for the optical properties. In these cases new initial parameters were attempted. Unique values for all parameters that corresponded to physiological values for the optical properties were always obtained.

This approach presented results comparable to the use of more traditional models, such as the diffusion theory com-

Table 2 Values of *a*, *b*, f_v, SO_2, *A*, *B*, and optical properties at 630 nm for normal sites of PDT patients.

Patent No.	Site	a (cm^{-1})	b (–)	f_v (%)	SO_2 (%)	A (cm^{-1})	B (nm^{-1})	$\mu_s'^{630}$ (cm^{-1})	μ_a^{630} (cm^{-1})	δ^{630} (mm)
	1	7093	0.98	0.98	59	1565	0.013	13.0	0.64	2.0
E1	2	75 318	1.36	0.73	59	576	0.010	12.1	1.10	1.5
	3	42 395	1.30	0.79	55	544	0.010	10.0	1.11	1.6
	1	163 662	1.53	1.57	41	164	0.008	8.3	0.78	2.2
E2	2	114 857	1.52	4.46	58	2773	0.014	6.4	1.10	2.0
	3	329 851	1.69	3.59	36	3183	0.014	6.1	1.20	1.9
	1	31 163	1.33	2.26	78	1426	0.013	6.0	0.64	2.8
E3	2	10 005	1.11	4.28	74	4995	0.017	7.8	0.56	2.7
	3	75 554	1.46	2.12	62	2700	0.014	6.4	0.69	2.6
	1	99 004	1.51	4.23	59	945 042	0.025	5.9	0.67	2.8
E4	2	262 333	1.62	3.15	91	53	0.007	7.7	1.07	1.9
	3	29 061	1.34	2.72	52	186 929	0.022	5.3	0.59	3.1
	1	676 216	1.74	3.33	84	131	0.008	9.3	1.21	1.6
L1	2	47 908	1.46	2.58	43	17	0.003	4.0	2.97	1.3
	3	81 315	1.40	3.30	52	9253	0.016	9.6	0.95	1.8
	1	71 777	1.45	2.21	79	117	0.008	6.2	0.95	2.2
L2	2	47 726	1.37	5.79	60	61 024	0.019	7.0	1.07	2.0
	1	122 809	1.49	0.52	98	2987	0.013	8.5	1.04	1.8
O1	2	70 452	1.37	1.74	60	3188	0.013	10.1	0.99	1.7
	3	324 176	1.60	0.84	76	6079	0.014	10.9	0.94	1.7

Table 3 Values of *a*, *b*, f_v, SO_2, *A*, *B*, and optical properties at 630 nm for tumor sites of PDT patients.

Patent No.	Site	a (cm^{-1})	b (–)	f_v (%)	SO_2 (%)	A (cm^{-1})	B (nm^{-1})	$\mu_s'^{630}$ (cm^{-1})	μ_a^{630} (cm^{-1})	δ^{630} (mm)
	1	704 706	1.75	11.1	16	7	0.005	8.7	3.02	1.0
E1	2*	704 706	1.75	3.89	33	16	0.005	8.7	1.65	1.4
	3*	704 706	1.75	8.75	25	9	0.005	8.7	2.38	1.1
	1	100 421	1.49	0.91	2	745	0.011	6.8	0.99	2.1
E2	2	306 758	1.63	4.76	42	5939	0.014	8.2	1.48	1.5
	3	241 450	1.53	5.83	18	4073	0.013	13.0	2.60	0.9
	1	10 019	1.13	6.41	0	394 768	0.023	6.7	1.94	1.4
E3	2*	10 019	1.13	2.57	59	189 758	0.023	6.7	0.43	3.3
	3*	10 019	1.13	8.20	7	0.79	0.023	6.7	2.24	1.3
	1	30 702	1.34	7.71	55	5 083 944	0.028	5.5	1.25	2.0
E4	2	139 231	1.50	5.53	60	1 405 882	0.026	8.8	0.83	2.0
	3	88 879	1.57	3.86	46	177 409	0.022	3.6	0.85	3.0
	1	1 169 888	1.82	0.97	54	44	0.006	9.7	1.14	1.6
L1	2	215 957	1.62	4.04	64	712	0.012	6.3	0.97	2.2
	3†	586 656	1.74	30.9	100	817	0.009	8.0	3.85	0.9
	1	109 379	1.42	2.87	38	2699	0.012	11.5	2.40	1.0
L2	2†	123 227	1.44	9.66	32	2903	0.011	11.5	4.88	0.6
	3	138 920	1.46	2.80	47	1441	0.010	11.5	2.60	1.0
	1	61 291	1.40	2.17	62	683	0.012	7.5	1.29	1.7
O1	2	9551	1.07	3.35	63	129 137	0.023	9.8	1.17	1.6
	3	17 324	1.17	2.92	58	54 476	0.021	9.0	1.26	1.6

* Assumes *a*, *b*, and *B* from site 1.

† Assumes *a*, *b*, and *B* based on average μ_s' and μ_a^{dry} of other two sites.
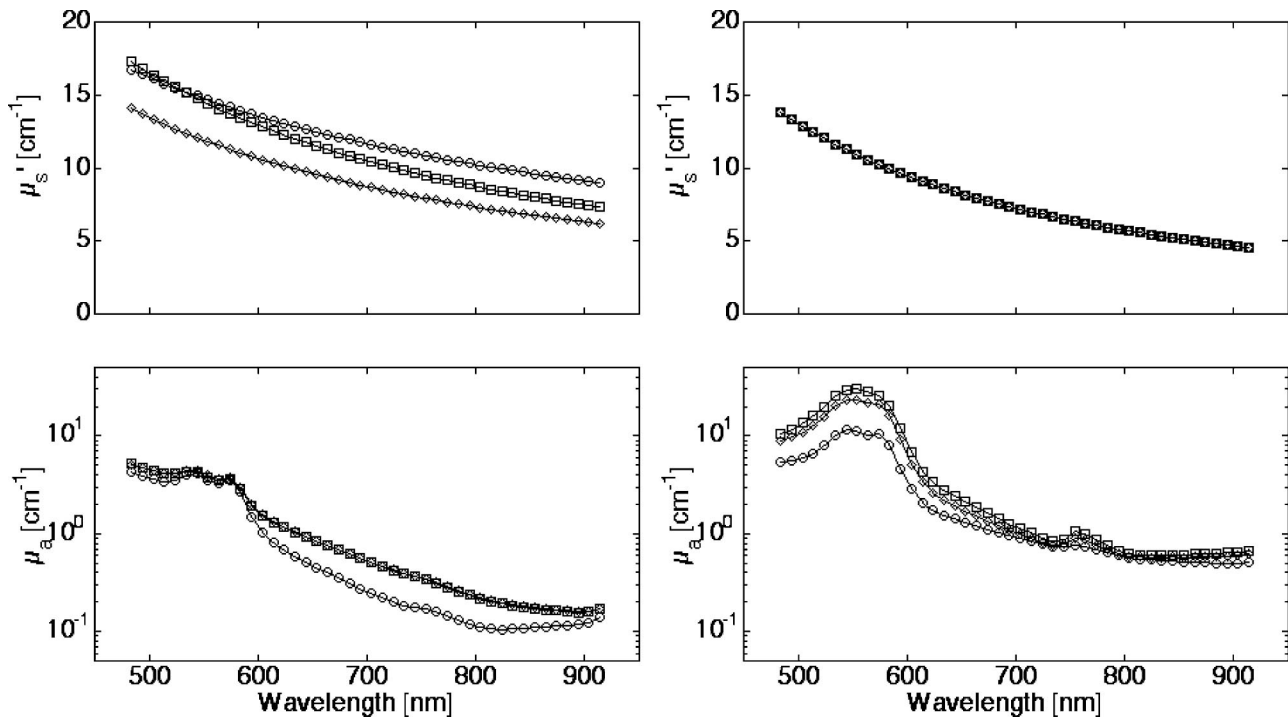
Fig. 14 Optical properties of three normal sites and three tumor sites from patient No. E1. (Top) Reduced scattering coefficient. (Bottom) Absorption coefficient. Identical reduced scattering coefficients are obtained for all three tumor sites (see text).

bined with adding doubling for *in vitro* measurements as shown in Fig. 13. Disagreement was found in the spectra below 650 nm as it should be expected since diffusion theory fails when the reduced mean free path $[1/(\mu_a + \mu_s')]$ is comparable with the source-detector separation and when μ_a is comparable to μ_s'. Literature values for bovine muscle at 630 nm have μ_s' ranging from 4.4 to 7 cm^{-1} (Ref. 33) and μ_a ranging from 0.4 to 3.5 cm^{-1},[33] which are in agreement with the results obtained with the method presented in this study.

Residuals shown in Figs. 14(a)–14(f) were typical for all the sites measured and were always below 20% for most spectral ranges. Recall that some of the tumor sites were blood saturated (highlighted in Table 3) and assumptions of different tumors sites having the same μ_s' and same μ_a^{dry} were made. These results obtained for blood saturated sites should be con-

Table 4 Mean and standard deviations for f_v, SO$_2$, μ_a, μ_s', and δ at 630 nm. PDT patient data exclude measurements in skin (see text).

	Non-PDT normal	PDT normal	PDT tumor
f_v (%)	1.72 ± 0.93	2.60 ± 1.49	6.15 ± 6.34
SO$_2$ (%)	54 ± 10	65 ± 16	42 ± 24
μ_s' at 630 nm (cm^{-1})	7.7 ± 1.5	7.8 ± 2.3	8.4 ± 2.3
μ_a at 630 nm (cm^{-1})	0.80 ± 0.23	0.87 ± 0.22	1.87 ± 1.10
δ at 630 nm (mm)	2.3 ± 0.5	2.2 ± 0.5	1.6 ± 0.7

sidered only as estimates since the earlier assumptions were not experimentally proved. Nevertheless all blood saturated sites presented higher values of blood content, as expected. Blood oxygen saturation results were compromised in these sites since it relied mainly on the presence and magnitude of the deoxy-blood peak at 780 nm which is a small spectral feature compared to the absorption bands in the 500–600 nm range. It should be noted that the results for SO$_2$ in this work represent the mixed arterio-venous blood oxygen saturation which explain the low average values shown in Table 4 as opposed to the arterial blood oxygen saturation typically in the 90%–98% range. Reconstruction of the optical properties for all sites is direct with the use of values in Tables 1–3 and Eqs. (7)–(9).

Comparison of non-PDT normal, PDT normal, and PDT tumor patients are given in Tables 3 and 4. The mean value of f_v and SO$_2$ were respectively 50% and 20% greater for the PDT normal compared to the non-PDT normal with p values of <0.03 and <0.01. In contrast the absorption coefficient at 630 nm was statistically the same for both patient populations. The reason for this discrepancy may be the fact that the non-PDT normal population was composed of only esophageal tissue whereas the PDT normal population was composed of esophageal tissue as well as oral and bronchial mucosa. Blood fraction of PDT tumor sites was more than two times greater than in PDT normal tissues ($p<0.02$). This is probably due to the increased vascularization typical of tumor tissue.[34] The increased blood fraction accounted for a twofold higher absorption coefficient ($p<0.001$). Blood oxygen saturation was 50% lower ($p<0.003$) for PDT tumor compared to PDT normal sites. No significant difference was found between non-PDT normal, PDT normal, and PDT tumor reduced scattering
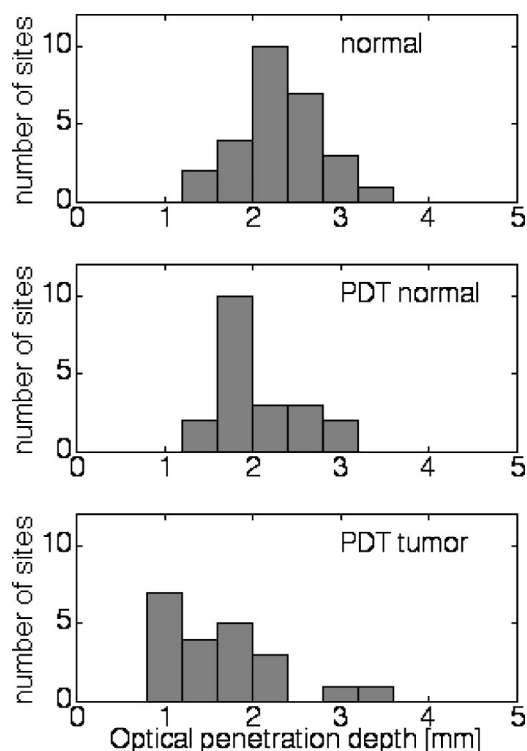
Fig. 15 Histograms of the optical penetration depth at 630 nm in normal tissue for non-PDT and in normal and tumor tissue for PDT patients.

coefficient. As a consequence the optical penetration depth (δ) for PDT tumor patients was 38% smaller than δ for the PDT normal patients ($p<0.002$). Reduced scattering and absorption coefficients determined in this work are comparable to results obtained by other authors for esophagus ($\mu_s'=7.0 \pm 2.3\,\mathrm{cm}^{-1}$ and $\mu_a=0.27\pm0.14\,\mathrm{cm}^{-1}$ at 630 nm),[17] bronchial submucosa ($\mu_s'=12.4\pm0.7\,\mathrm{cm}^{-1}$ and $\mu_a=1.8 \pm0.2\,\mathrm{cm}^{-1}$ at 633 nm)[35] and bronchial tumor ($\mu_s'=12.5 \pm0.7\,\mathrm{cm}^{-1}$ and $\mu_a=1.2\pm0.2\,\mathrm{cm}^{-1}$ at 633 nm).[35]

This paper established an experimental method for determination of optical properties *in vivo* based on an empirical light transport function. Although the method was probe specific similar functions could be derived for any probe configuration if proper calibration is performed. Blood perfusion was the main variable accounting for differences in the optical properties on the studied tissues. The fraction of blood ranged from 0.1% to 30%. Although normal tissue showed an increased reduced scattering coefficient and tumor tissue showed an increased absorption coefficient for a given patient, the patient-to-patient variability was considerable. That variability explained the large range of optical penetration depth (0.6–3.6 mm) obtained for both normal and tumor tissues.

Acknowledgments

References

1. V. G. Peters, D. R. Wyman, M. S. Patterson, and G. L. Frank, "Optical properties of normal and diseased human breast tissues in the visible and near infrared," *Phys. Med. Biol.* **35**, 1317–1334 (1990).
2. S. L. Jacques, "Laser-tissue interactions: photochemical, photothermal, photomechanical," *Surg. Clin. North Am.* **72**, 531–558 (1992).
3. J. W. Pickering, S. Bosman, P. Posthumus, P. Blokland, J. F. Beek, and M. J. C. van Gemert, "Changes in the optical properties (at 632.8 nm) of slowly heated myocardium," *Appl. Opt.* **32**, 367–371 (1993).
4. M. S. Patterson, E. Schwartz, and B. C. Wilson, "Quantitative reflectance spectrophotometry for the noninvasive measurement of photosensitizer concentration in tissue during photodynamic therapy," in *Photodynamic Therapy: Mechanisms*, T. J. Dougherty, Ed., *Proc. SPIE* **1065**, 115–122 (1989).
5. C. M. Gardner, S. L. Jacques, and A. J. Welch, "Fluorescence spectroscopy of tissue: recovery of intrinsic fluorescence from measured fluorescence," *Appl. Opt.* **35**, 1780–1792 (1996).
6. D. R. Braichotte, G. A. Wagnieres, R. Bays, P. Monnier, and H. E. van den Bergh, "Clinical pharmacokinetics studies of Photofrin by fluorescence spectroscopy in the oral cavity, the esophagus and the bronchi," *Cancer* **75**, 2768–2778 (1995).
7. S. L. Jacques, "Simple theory, measurements, and rules of thumb for dosimetry during photodynamic therapy," in *Photodynamic Therapy: Mechanisms*, T. J. Dougherty, Ed., *Proc. SPIE* **1065**, 100–108 (1989).
8. S. A. Prahl, M. J. C. van Gemert, and A. J. Welch, "Determining the optical properties of turbid media by using the adding-doubling method," *Appl. Opt.* **32**, 559–568 (1993).
9. J. W. Pickering, C. J. M. Moes, H. J. C. M. Sterenborg, S. A. Prahl, and M. J. C. van Gemert, "Two integrating spheres with an intervening scattering sample," *J. Opt. Soc. Am. A* **9**, 621–631 (1992).
10. J. W. Pickering, S. A. Prahl, N. van Wieringen, J. F. Beek, H. J. C. M. Sterenborg, and M. J. C. van Gemert, "Double-integrating-sphere system for measuring the optical properties of tissue," *Appl. Opt.* **32**, 399–410 (1993).
11. E. M. Sevick, B. Chance, J. Leigh, S. Nioka, and M. Maris, "Quantitation of time- and frequency resolved optical spectra for the determination of tissue oxygenation," *Anal. Biochem.* **195**, 330–351 (1991).
12. S. Fantini, M. A. Francechini-Fantini, J. S. Maier, S. A. Walker, B. Barbieri, and E. Gratton, "Frequency-domain multichannel optical detector for noninvasive tissue spectroscopy and oximetry," *Opt. Eng.* **34**, 32–42 (1995).
13. M. S. Patterson, B. Chance, and B. C. Wilson, "Time resolved reflectance and transmittance for the noninvasive measurements of optical properties," *Appl. Opt.* **28**, 2331–2336 (1989).
14. S. Andersson-Engels, R. Berg, A. Persson, and S. Svanberg, "Multispectral tissue characterization with time-resolved detection of diffusely scattered white light," *Opt. Lett.* **18**, 1697–1699 (1993).
15. A. A. Oraevsky, S. L. Jacques, and F. K. Tittel, "Measurement of tissue optical properties by time-resolved detection of laser-induced transient stress," *Appl. Opt.* **36**, 402–415 (1997).
16. T. J. Farrell and M. S. Patterson, "A diffusion theory model of spatially resolved, steady-state diffuse reflectance for the noninvasive determination of tissue optical properties *in vivo*," *Med. Phys.* **19**, 879–888 (1992).
17. R. Bays, G. Wagnieres, D. Robert, D. Braichotte, J.-F. Savary, P. Monnier, and H. van den Bergh, "Clinical determination of tissue optical properties by endoscopic spatially resolved reflectometry," *Appl. Opt.* **35**, 1756–1766 (1996).
18. S. L. Jacques, "Modeling light transport in tissue," in *Biomedical Optical Instrumentation and Laser-Assisted Biotechnology*, A. M. Verga Scheggi et al., Eds., pp. 21–32, Kluwer Academic, The Netherlands (1996).
19. W. J. Ride, "The scattering of light by turbid media—part I," *Proc. R. Soc. London, Ser. A* **131**, 451–464 (1931).
20. W. G. Egan and T. Hilgeman, "*In situ* separation of scattering and absorption in fluids," *Appl. Opt.* **20**, 727–729 (1981).
21. P. R. Bargo, S. A. Prahl, and S. L. Jacques, "Optical properties effects upon the collection efficiency of optical fibers in different probe configurations," *IEEE J. Sel. Top. Quantum Electron.* **9**, 314–321 (2003).
22. P. R. Bargo, S. S. Prahl, and S. L. Jacques, "Collection efficiency of a single optical fiber in turbid media," *Appl. Opt.* **42**, 3187–3197 (2003).

23. S. A. Prahl, "Light Transport in Tissue," PhD dissertation, University of Texas, Austin, TX (1988).
24. B. C. Wilson, "Measurement of tissue optical properties: methods and theories," in *Optical-Thermal Response of Laser Irradiated Tissue*, A. J. Welch and M. J. C. van Gemert, Eds., Chap. 8, pp. 233–274, Plenum, New York (1995).
25. I. S. Saidi, S. L. Jacques, and F. K. Tittel, "Mie and Rayleigh modeling of visible-light scattering in neonatal skin," *Appl. Opt.* **34**, 7410–7418 (1995).
26. S. A. Prahl, "Optical properties Spectra" [Online] Available: http://omlc.ogi.edu/spectra/
27. L. S. Saidi, "Transcutaneous optical measurement of hyperbilirubinemia in neonates," PhD dissertation, Rice University, Houston, TX (1992).
28. W. M. Star, "Diffusion theory of light transport," in *Optical-Thermal Response of Laser Irradiated Tissue*, A. J. Welch and M. J. C. van Gemert, Eds., Chap. 6, pp. 131–206, Plenum, New York (1995).
29. D. S. Moore and G. P. McCabe, *Introduction to the Practice of Statistics*, 2th ed., pp. 529–557, W. H. Freeman and Company, New York (1993).
30. Endoscopes Catalog, Olympus America, Inc., [Online] Available: http://www.olympusamerica.com/msg_section/msg_gastro_g.asp (2003).
31. T. P. Moffitt and S. A. Prahl, "Sized-fiber reflectometry for measuring local optical properties," *IEEE J. Sel. Top. Quantum Electron.* **7**, 952–958 (2001).
32. T. P. Moffitt and S. A. Prahl, "The specular reflection problem with a single fiber for emission and collection," *Proc. SPIE: Saratov Fall Meeting* (2002).
33. W.-F. Cheong, S. A. Prahl, and A. J. Welch, "A review of the optical properties of biological tissue," *IEEE J. Quantum Electron.* **26**, 2166–2185 (1990).
34. A. Abramsson, O. Berlin, H. Papayan, D. Paulin, M. Shani, and C. Betsholtz, "Analysis of mural cell recruitment to tumor vessels," *Circulation* **105**, 112–117 (2002).
35. J. Qu, C. MacAulay, S. Lam, and B. Palcic, "Optical properties of normal and carcinomatous bronchial tissue," *Appl. Opt.* **33**, 7397–7405 (1994).